



LAWRENCE
LIVERMORE
NATIONAL
LABORATORY

Fracture, failure and compression behaviour of a 3D interconnected carbon aerogel (Aerographite) epoxy composite.

S. Chandrasekaran, W. V. Liebig, M. Mecklenberg, B. Fiedler, D. Smazna, R. Adelung, K. Schulte

October 16, 2015

Fracture, failure and compression behaviour of a 3D interconnected carbon aerogel (Aerographite) epoxy composite.

Disclaimer

This document was prepared as an account of work sponsored by an agency of the United States government. Neither the United States government nor Lawrence Livermore National Security, LLC, nor any of their employees makes any warranty, expressed or implied, or assumes any legal liability or responsibility for the accuracy, completeness, or usefulness of any information, apparatus, product, or process disclosed, or represents that its use would not infringe privately owned rights. Reference herein to any specific commercial product, process, or service by trade name, trademark, manufacturer, or otherwise does not necessarily constitute or imply its endorsement, recommendation, or favoring by the United States government or Lawrence Livermore National Security, LLC. The views and opinions of authors expressed herein do not necessarily state or reflect those of the United States government or Lawrence Livermore National Security, LLC, and shall not be used for advertising or product endorsement purposes.

**Fracture, failure and compression behaviour of a 3D interconnected carbon aerogel
(Aerographite) epoxy composite.**

*Swetha Chandrasekaran^{*1}, Wilfried V. Liebig², Matthias Mecklenberg², Bodo Fiedler², Daria Smazna³ Rainer Adelung³, Karl Schulte².*

¹ Lawrence Livermore National Laboratory, 7000 East Avenue, Livermore, California 94550, USA.

² Institut für Kunststoffe und Verbundwerkstoffe, Technische Universität Hamburg-Harburg, Denickestrasse, 15, D-21073 Hamburg, Germany.

³ Institut für Materialwissenschaft - Funktionale Nanomaterialien, Christian-Albrechts-Universität zu Kiel, Kaiserstrasse 2, 24143 Kiel, Germany.

* Corresponding author: Tel: +1-925-424-6816. Fax: +1-925-423-7040. Email address: Chandrasekar2@llnl.gov (S.Chandrasekaran)

Abstract

Aerographite (AG) is a mechanically robust, lightweight synthetic cellular material, which consists of a 3D interconnected network of tubular carbon [1]. The presence of open channels in AG aids to infiltrate them with polymer matrices, thereby yielding an electrical conducting and lightweight composite. Aerographite produced with densities in the range of 7-15 mg/cm³ was infiltrated with a low viscous epoxy resin by means of vacuum infiltration technique. Detailed morphological and structural investigations on synthesized AG and AG/epoxy composite were performed by scanning electron microscopic techniques. The present study investigates the fracture and failure of AG/epoxy composites and its energy absorption capacity under compression. The composites displayed an extended plateau region when uni-axially compressed, which lead to an increase in energy absorption of ~133 % per unit volume for 1.5 wt% of AG, when compared to pure epoxy. Preliminary results on fracture toughness showed an enhancement of ~19 % in K_{IC} for AG/epoxy composites with 0.45 wt% of AG. Observations of fractured surfaces under scanning electron microscope gives evidence of pull-out of arms of AG tetrapod, interface and inter-graphite failure as the dominating mechanism for the toughness improvement in these composites. These observations were consistent with the results obtained from photoelasticity experiments on a thin film AG/epoxy model composite.

Keywords: Nanocomposites (A); Fracture toughness (B); Mechanical properties (B); Fractography (D) and Scanning electron microscopy (D).

1 Introduction

Ever since the discovery of graphene - a two dimensional monolayer of sp^2 hybridized carbon atoms, researchers have used graphene as a filler in polymer nano-composites to increase the mechanical, electrical and thermal properties of the polymeric matrix [2]. Although an ideal defect free graphene exhibits better intrinsic properties such as modulus, electrical and thermal conductivity, the properties largely depend on structural defects, number of layers and lateral size of the graphene flakes [3,4].

Though graphene polymer nano-composites exhibit improved properties, utilization of graphene's full potential is still a challenge due to the problem of dispersion [5,6]. The high specific surface area of graphene leads to van der Waals forces between the graphene sheets thereby leading to stacking of graphene sheets. This in turn leads to a poor dispersion of graphene sheets in the polymeric matrix that limits the improvement in material properties of nano-composites. It was shown by Young et al., that the stacking of graphene layers can be detrimental and that the modulus of mono-layer, bi-layer and tri-layer graphene decreases from 1 TPa down to 600 GPa [7]. Another factor that influences the properties of the composite is the amount of filler dispersed in the polymeric matrix. At lower filler content, the polymeric chains restrict formation of a percolated network by the nano-filler and a higher filler content is required to form a percolated network. However, with increasing filler content, the viscosity of the polymeric matrices increases and causes difficulties in manufacturing the nano-composites.

A three-dimensional lightweight foam like material, containing a highly interconnected microstructure, high degree of flexibility and strength is able to address the limitations such as poor dispersion and re-agglomeration observed with graphene sheets [8]. These graphene foams

are reported under different nomenclature across the scientific community as graphene aerogels, graphene foam, graphene sponge, Aerographite and porous carbon. Potential uses for these nano-carbon based foams and porous structures include low-density, high-conductivity electrodes for 'super-capacitors' [9], adsorption/desorption of water contaminations [10], energy storage devices [11] and for electro-chemical sensing [12]. Various methods of manufacture have been used to create such carbon-based structures, including chemical vapour deposition onto porous nickel foams, direct drying of graphene oxide hydrogels and by deposition of graphene oxide over polyurethane foams [13].

For infiltration of these graphene foams with polymeric matrix, generally graphene foam grown over Ni foam in a CVD reactor or reduced graphene foam from graphene oxide were mostly used. Jia et al., reported improvement in toughness by 78 % for 0.1 wt% loading of graphene foam (GF), along with improved flexure modulus and strength by 53 % and 38 % resp. for 0.2 wt% [14]. Chen et al., prepared a light weight graphene foam/PDMS composite having a density of 0.06 g/cm^3 and the composite showed an effective EMI shielding of 30 dB for less than 0.8 wt% of filler loading. The composite exhibited excellent flexibility by retaining the shielding effectiveness even after bending it by 10, 000 times [15,16]. Li et al., investigated the electrical conductivity of graphene sponge infiltrated with epoxy and observed an increase in electrical conductivity from 0.2 to 1.7 S/m [17]. Chen et al., prepared the graphene foam/epoxy composite showing a maximum conductivity of 196 S/m at 2.5 vol.% filler loading, and a rather low percolation threshold of 0.18 vol.% [18]. In another study, Misra et al., studied the compressive behaviour of graphene foam/PDMS composite. The energy absorption in these composites increased to 0.15 MJ/mm^3 from 0.04 MJ/mm^3 at 20 % compressive strain when compared with neat graphene foam. In addition, the compressive modulus showed a 7-fold increase for graphene

foam/PDMS composite when compared with neat graphene foam. This indicates the use of these composite as shock absorbers, cushions, dampers etc. [19]. Polymer based graphene foams (PGFs) exhibited a maximum compressibility of 90 % and showed a high electromechanical stability even after 300 bending cycles [20]. Zhao et al., prepared polypyrrole (PPy)-Graphene foam through in-situ preparation method and demonstrated a highly compression-tolerant graphene-based super capacitor. The specific capacitance of PPy-G foams was calculated to be 350 F/g, which is much higher than both PPy film and pure graphene foam [21]. Lao et al., tested graphene foam/PDMS composite for its application as a strain/pressure sensor. The composite exhibited 90% resistance change with only 10 % compressive strain, and at 30 % strain the resistance change was 850 % and thus, exhibiting a tuneable sensitivity [22]. Kim et al., reported anisotropy in the electrical and mechanical properties in graphene aerogel/epoxy composite by freeze drying graphene oxide aerogels and by subsequent infiltration with epoxy. The enhancement in fracture toughness was 64 % for 1.4 wt% filler content when the crack propagates perpendicular to the alignment of graphene layers. A maximum difference of 113 % in fracture toughness in these composites when measured in parallel and transverse alignment of the graphene sheets [23]. Graphene nano-ribbon (GNR) aerogels prepared by unzipping nanotubes also exhibited improved properties when infiltrated with PDMS. A 10-fold increase in toughness was observed in these composite for 0.87 wt% of GNR aerogel when compared with PDMS [24].

In the present work, we investigate one such 3D graphene interconnected structure - “Aerographite” infiltrated with an epoxy matrix. The work aims to prepare an AG/epoxy composite without damaging the interconnected network of AG and to study its mechanical properties. The main aim of our work is to understand the failure mechanism in these

composites and in addition to observe the interaction of crack with an AG agglomerate in model composite through photoelasticity.

2 Materials and synthesis of AG

For the infiltration of Aerographite, a low viscous epoxy system (epoxy resin (Rim 135) and a hardener (Rim 137) from Momentive) in the mass ratio of 100:30 was used. After the manually mixing of the resin and the hardener for 15 minutes, the resin mixture was degassed to remove air bubbles, prior to infiltration. In this study, five cylindrical Aerographite samples of 2 cm³ in volume (diameter 12 mm and height 14 mm) was synthesised in different batches from 3D interconnected and highly porous ZnO templates in a chemical vapour deposition (CVD) process which is described in detail in previous work [1]. During the synthesis, the carbon-feeding rate is a key parameter to adjust the resulting density of AG (i.e., wall-thickness of graphitic layers of AG). Here, the injection of toluene was kept at 6 ml/h/g to yield the closed shell variant of Aerographite. These closed shell morphology of AG has a higher density (9-15 mg/cm³) and this morphology is necessary to withstand the potential collapse during vacuum infiltration of epoxy.

2.2 Preparation of composite

The composite was prepared by injecting a low viscosity epoxy into Aerographite using vacuum injection method. Prior infiltration, Aerographite was kept under vacuum at 50 °C to remove moisture; the resin mixture was also kept at 50 °C to lower the viscosity, as it will ease the injection process. This method removes the need to shear the matrix to disperse the nanoparticles by milling or sonication to preserve the 3D interconnected structure of the Aerographite. AG samples were then placed into an aluminum mold and the whole setup was placed inside a vacuum desiccator. Epoxy resin mixture was then injected into the mold through

a syringe at an injection rate of 0.1 ml/min. The whole infiltration process took place under vacuum at a pressure 9 mbar. See Fig. 1 for a schematic illustration of the fabrication process.

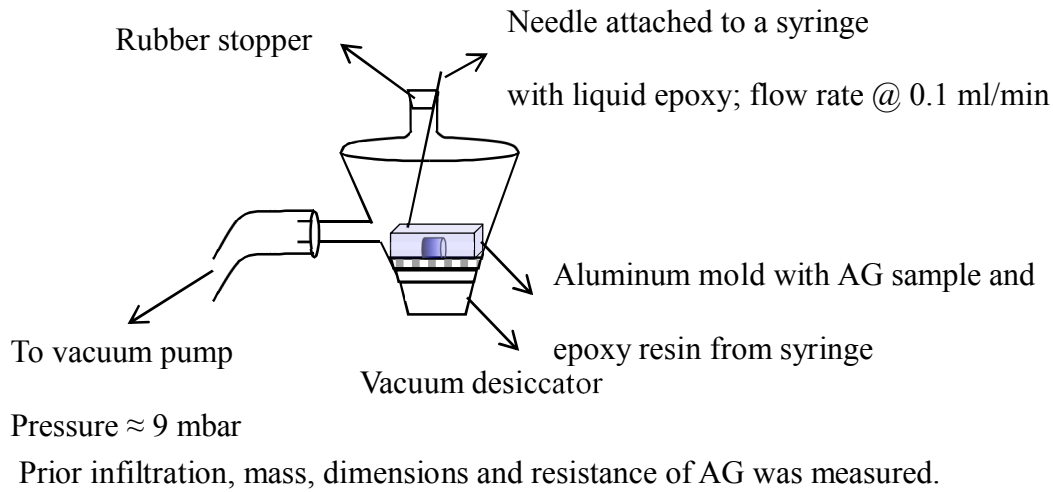


Figure 1: A schematic illustration and a photograph of AG/epoxy composite preparation.

During the capillary action, the resin flows through the open tubular arms of Aerographite, and the process was terminated when the Aerographite is completely saturated and covered by a layer of epoxy on all sides. The epoxy infused Aerographite was subjected to room temperature curing for 24 h and was then post cured at 80 °C for 15 h. A larger sample size was not achievable due to current limitations of the Aerographite after the CVD process. Similar infiltration method is reported in literature where the aerogel is completely soaked with epoxy and is left in vacuum overnight [25]. Note that, by infiltrating the pores of the Aerographite with epoxy, it is expected that the lightweight and conductive properties of the Aerographite will be retained, whilst the stiffness and hardness of the epoxy will protect the AG's delicate open structure and allow a greater number of uses for the composite. It is not known if Aerographite is truly an open-celled foam: that is, whether all tetrapod arms are open, allowing for complete infiltration of liquid epoxy.

2.3 Fracture toughness tests

The fracture toughness (K_{IC}) was evaluated by using the Zwick Roell Z010 Universal testing machine in three-point end notch bending (SEN-3PB) test mode, which has the load cell capacity of 10kN. The SEN-3PB test was carried out according to ASTM D5045. Rectangular specimens were cut from the cured plates and were polished down to the dimensions required for testing. The dimensions of the specimens were 36 mm (length) x 8 mm (height) x 4 mm (thickness). The distance between the supporting rollers of the 3-point bending test was 32 mm. The crosshead speed was 10 mm/min. The samples were pre-cracked before testing such that the ratio of specimen height to crack length was between 0.45-0.55 as per the standard. Further detailed information is provided in supplementary information.

2.4 Microscopic and Raman analysis

Scanning electron microscopy (SEM) was used to analyse the fracture surface of AG/epoxy composite to understand the failure mechanism in these composites. The fracture surfaces were observed using a FE-SEM (Zeiss LEO 1530 Gemini, Carl Zeiss Inc.) by applying an acceleration voltage of 1 kV without sputtering. Here, two kinds of detectors were used for SEM observation as necessary. The SE2 detector was used for the fracture surface morphology, and the in-lens detector was used to view the as-prepared Aerographite. For transmission optical observations, the outer layer of epoxy was ground off until the Aerographite/epoxy composite was at the surface. Transmission optical observations were made on thin slices of AG/epoxy, which was polished down to 80 μm thick from the bulk composite. Additionally a simple notch specimen (see supplementary info Fig. S4) was tested using a test jig fitting in a transmission light microscope with integrated photoelasticity. The set-up of the photoelasticity is configured to visual the isochromatic fringes as described by Patterson and Wang [26].

Raman spectra was recorded to confirm the presence of graphitic layers in the fracture surface and was recorded with a Horiba Jobin Yvon HR800 spectrometer. The spectra were taken using He-Ne laser with a wavelength of 638.2 nm and the spectra was recorded in the range of 100-3000 cm^{-1} .

2.5 Compression tests

The prepared samples of Aerographite/epoxy composite and pure epoxy were then tested in a Zwick Universal Testing Machine with a maximum load of 100 kN available, loading at a rate of 1.3 mm/min. The linear displacement of the sample was recorded, allowing the strain to be calculated using its uncompressed length. The cured AG/epoxy composites were cut to 5.0 x 5.0 x 10.0 mm^3 cuboids, in accordance with ASTM standard D695-02a for isotropic materials, and polished so that the ends of the samples were accurate to 25 μm . This minimized frictional forces at the interface between sample and plates of the compression machine. This small sample size was chosen to match the volume of the composite samples produced to give an equal probability of each having defects large enough to cause failure. Two polyethylene (PE) sheets were placed, without securing, between the sample and the loading plates to minimise friction between the sample ends and the loading plates, thus preventing regions of unstressed material at the plates [27]. Altogether 20 cuboid samples of the composite were tested in compression with two different batches of AG whose average densities are $9.36 \pm 2.68 \text{ mg/cm}^3$ and $14.07 \pm 3.1 \text{ mg/cm}^3$ respectively.

3 Results

3.1 Morphology of as-prepared AG

The morphology of as-prepared AG exhibited variation in their structure upon inspection of cross-sections of the samples in the SEM (Fig. 2), with some regions estimated to be comprised

of ~30 % graphitic plates rather than hollow tubes. The size and shape of the ZnO template is directly transferred to the AG synthesised from CVD process.

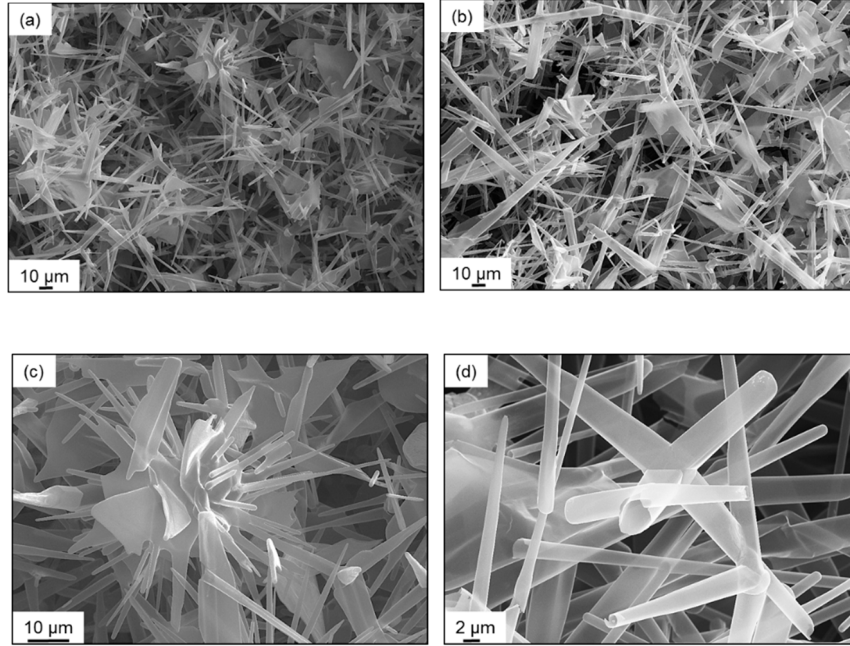


Figure 2: Scanning electron micrograph of as-prepared AG showing (a) variation in the structure with large graphitic plates, (b) arms of varying thickness along their length (c) multiple arms connected to a graphitic plate, (d) the open ends of the hollow AG tetrapod that enables infiltration.

In Fig 2c, multi-arms and sheet-like particles can also be observed besides defined geometrical tetrapods. In general, all tetrapods are in a length scale of ~30-50 µm with several interpenetrating connections between them (Figs. 2a and b). The proportion of each morphology seen in Fig. 2 is determined by the ZnO template architecture used and the position of the sample relative to the gas flow during the CVD synthesis, and therefore is currently beyond our control. However, it is worth noting that, the densest samples were chosen for imaging under SEM and hence represents the worst-case morphology for Aerographite. As observed in Fig. 2d, open ends of some of the AG arms along with the interconnections between the arms are considered to allow full filling of the inner volumes with epoxy which is later on observed in composite's

fracture surface too. The average wall thickness of AG arm was estimated to be ~ 53 nm, as found from SEM observations.

3.2 Morphology of the composite

The transmission optical micrograph shows that the 3D interconnected network of AG remains intact during the infiltration and curing process.

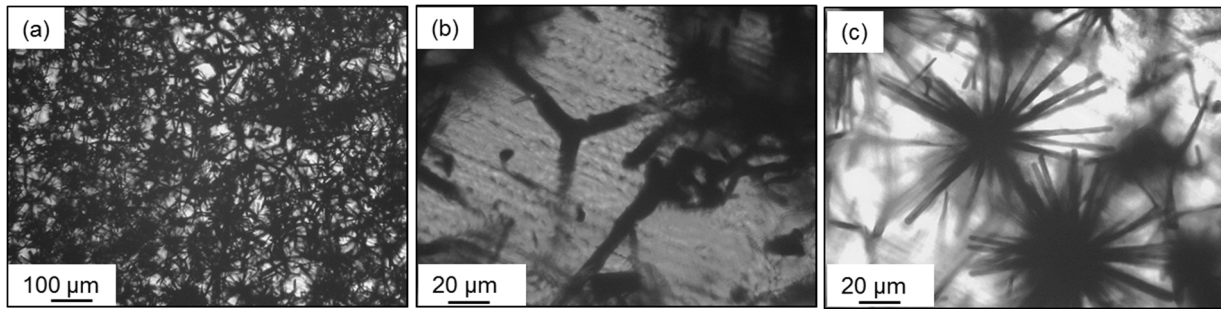


Figure 3: Transmission optical micrographs of AG/epoxy composite thin films (80 μm thick) (a) dense network of AG, (b) a single AG tetrapod and (c) a dense AG multipod embedded in epoxy matrix.

Fig. 3a, shows a dense 3D network of AG arms in the epoxy matrix, although the density of the network varies in the composite. Higher magnification micrographs (b) show a single AG tetrapod which connects to other dense networks and (c) shows a “sea-urchin” like morphology where several arms grow from a single point (present in ZnO template). These observations indicate that the infiltration technique adapted for these composites works well.

3.3 Fracture toughness SEN-3PB test

The fracture toughness of the AG/epoxy composite measured by SEN-3PB test is plotted as a function of weight percent of filler (0.3 to 1.1 wt%) of AG in Fig. 4. It is difficult in case of AG/epoxy composite to discuss in terms of filler content increase, as it is 3D interconnected structure. However, there is an increase in K_{IC} with the increase in weight percentage (wt%) of AG content in the composite.

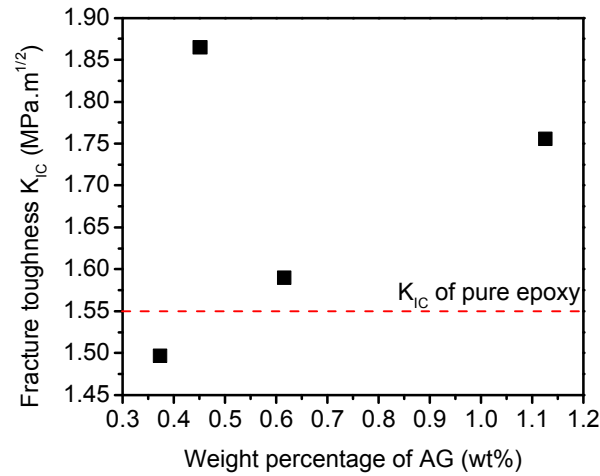


Figure 4: Fracture toughness of AG/epoxy composite as a function of weight percentage of AG.

This increase is only 13 % at 1.1 wt% of AG and when compared to conventional graphene/epoxy composite. However, the data at 0.45 wt% corresponding to K_{IC} increase of 19 % is an example on the quality of AG prior infiltration, and presence of a fewer number of pores during the infiltration process. Note that the K_{IC} of pure epoxy is 1.575 ± 0.062 MPa.m^{1/2}. As mentioned earlier, the infiltration process adapted to prepare the composite, can introduce some pores during vacuum infiltration even though, the rate of injection of resin is very slow. This indeed can severely affect the properties (especially K_{IC}). In addition, the overall properties of the composite is largely governed by the number of interconnects in the composite, wall thickness of the AG tetrapod and remnant ZnO present in AG after CVD process. Therefore, quality of AG and a pore free infiltration process can yield AG/epoxy composites even with increase in K_{IC} at lower filler concentrations that supports the anomaly in graph at 0.45 wt%.

3.4 Compression tests – Energy absorption

For compression testing, the geometry of the sample to be tested is generally cylindrical as it minimizes the number of points at which stress can concentrate. However, for the present study cubic samples were preferred due to the ability to polish accurately their flat surfaces. Thin PE

films were used on both sides of the samples, before testing to minimize friction while compression. The film allowed the stress applied by the machine to be distributed evenly over the sample's surface in contact with the plate, but had negligible effect on the elastic modulus of the samples during elastic compression. Early failure of composites, rather than densification, is a side effect of using the polymer film to decrease friction and prevent barrelling of the samples. Instead, the samples faces slipped and some shear stress was introduced, causing the samples to rotate so that their longest axis was no longer perpendicular to the machine's plates. This decreased the surface area, which experienced the load, and was found to be unavoidable if friction was to be reduced. Representative compressive stress-strain curve of pure epoxy, AG/epoxy for different weight percentage are shown in Fig. 5.

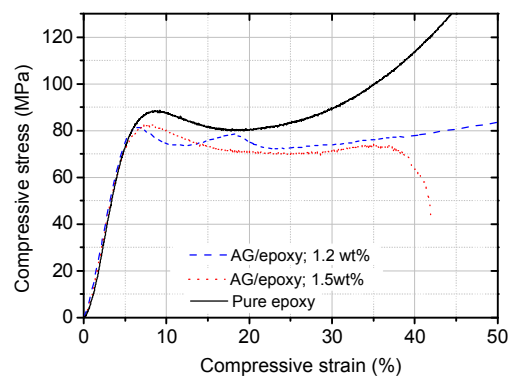


Figure 5: A comparison of the behaviours of AG/epoxy composites from different Aerographite batches, as well as pure epoxy, when subjected to uni-axial compression.

The composite samples exhibited several distinct regions in their stress-strain (σ - ϵ) curves plotted in compression. A linear elastic region, a plateau region and a densification region similar to the behaviour exhibited by conventional cellular solids. However, as explained earlier, the densification region cannot be observed for AG/epoxy composite. Nevertheless, all the samples exhibited the linear elastic deformation up to a strain of $\sim 7\%$ region followed by plastic yielding and a plateau region. Initial plastic yield occurred at strains of $\sim 7\%$, and post-yield softening

was observed in all samples. The average elastic modulus of the composites in compression was found to be lower than that of the epoxy indicating that, inclusion of the AG into the epoxy matrix causes a decrease in its stiffness. The yield stress (σ_y) of the composites, taken as the height of the first peak after the elastic region in curves with multiple peaks, was consistently lower, at an average of $\sigma_y = 82.59$ MPa compared to the pure epoxy, which had an average $\sigma_y = 88.68$ MPa. This is due to an increased weight fraction of brittle Aerographite giving a thinner interface of epoxy between arms, acting to increase the load experienced by the harder epoxy and decreasing the overall strength of the composite in compression.

It can be observed from the stress-strain curves that plateau region in composites are extended when compared with pure epoxy. This can be related to the compression behaviour exhibited by conventional cellular solids. According to Ashby et al., a cellular solid when subjected to compressive forces, exhibit a linear elastic region where, the material is subjected to a uniform deformation as the load increases, the stress value reaches a maximum and subsequently reaches a constant value indicating the plateau region [28]. The plateau region starts after the initial formation of shear crack, where there is a continued deformation at a constant stress value, which corresponds to the energy absorbed by the material when under compression. This is attributed to the crushing of the pulled out arms and peeling of the graphitic layers in the AG arms which opens up the enclosed hollow space providing more space for the compressing material to occupy. Several composites, particularly those created from the AG/epoxy 1.2 wt%, displayed multiple peaks (serration) in the plateau region of their stress-strain curves (Fig. 5), combined with a slight linear decrease in the applied stress with increasing strain. This kind of behaviour shows brittle failure of the AG, a phenomenon observed in closed-cell aluminium foams [21]. In brittle failure, a competition between the crushing of the infiltrated arms and the

densification of those arms already collapsed due to the application of the compressive stress; and pull-out of the infiltrated, uncollapsed arms as the introduction of shear stresses created tension in the sample. The brittle nature exhibited by AG/epoxy 1.2 wt% is also partly contributed from the remnant ZnO present in the AG after the CVD process. It must be noted that, the amount of remnant ZnO present after the CVD process is unknown and at present, it can only be qualitatively interpreted from the density of the AG.

The energy absorbed per unit volume during compression of each sample was found by integrating under the stress-strain curve for the composite. This value was then divided by the density of the sample, to find the energy absorbed per unit mass. In all cases, the energy absorbed by the AG/epoxy composite was higher than for the pure epoxy, showing an increase of 62 % and 151 % compared to the pure epoxy for different filler contents. Graph containing the energy absorbed per unit mass by pure epoxy and AG/epoxy can be found in supplementary information Fig. S2. The difference between the Ag/epoxy composites is thought to be due to an increased number of epoxy-infiltrated arms being pulled out of the epoxy matrix in AG/epoxy sample with 1.5 wt%.

4 Discussion

4.1 Failure mechanism in AG/epoxy composite

4.1.1 Fracture surface analysis after SEN- 3PB test

Fig. 6 shows the SEM micrographs of pure epoxy, and the epoxy resin toughened with Aerographite on both the sides of the fracture surface. The adjacent fracture surfaces are named as side A and side B for convenience. The image of side A and that of side B are generally symmetric in nature, and for the ease of comparison and viewing, the image of side B is electronically tilted by 180°. The dotted lines indicate the crack propagation direction from top to bottom.

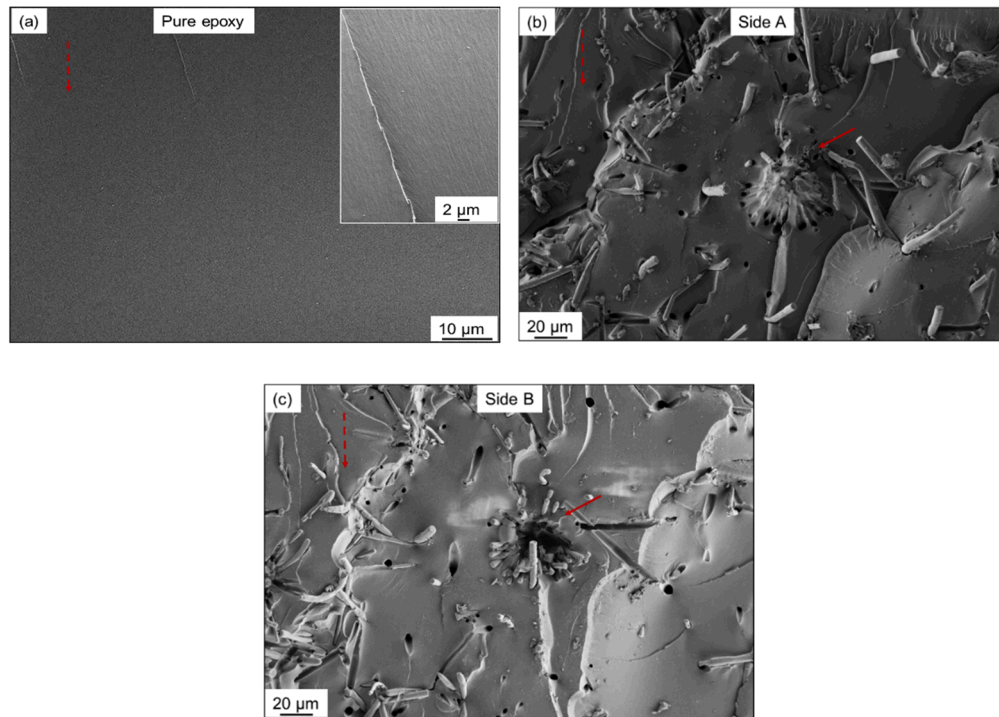


Figure 6: Representative fracture surfaces of AG/epoxy after SEN-3PB test (a) pure epoxy, (b) and (c) on both the fracture sides showing pull-out of AG tetrapods from a dense agglomerate indicated by solid red arrows.

Compared to pure epoxy fracture surface (Fig.6a), the AG/epoxy composite shows a rougher fracture surface, which reveals pull-out of the arms of Aerographite from the epoxy matrix. The brittle nature of epoxies is reflected in its smooth fracture surface with flow patterns of the resin observed at higher magnification. Indeed, the presence of AG in AG/epoxy composite as a mechanical reinforcement by inhibiting the crack and thereby toughening the matrix to a certain extent. The red arrow indicates one of the AG agglomerate, which consists of several arms, attached together giving the impression of a “sea-urchin” like appearance. In Fig 6a, all the arms that are pulled out from the matrix can be found on its counterpart as shown in Fig 6b. The pull-out of the AG tetrapods is one of the failure mechanism widely observed in fibre composites and

also in CNT/epoxy nano-composite. The arms of the tetrapod are pulled out from the matrix as the crack propagates and their cause is due to weak interfacial bonding. Whereas, for AG tetrapods, the pull-out seems to be very similar to that observed for CNT/epoxy composite which was elucidated by Gojny et al ., while investigating the failure mechanism of these composites [29]. The authors reported complete pull-out of CNTs in case of weak interface and CNT rupture, telescopic pull-out for a strong interface and partial de-bonding and bridging.

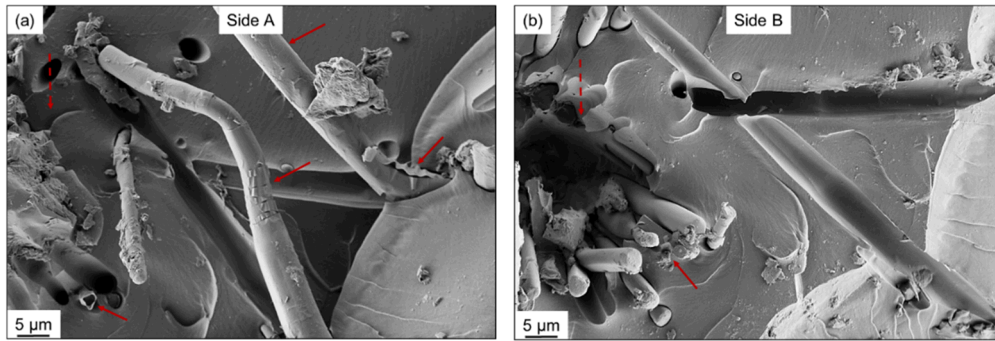


Figure 7: Scanning electron micrographs of AG/epoxy at higher magnification shows (a) an AG tetrapod being pulled out from the epoxy matrix and (b) impression of the pulled out arm on the other side of the fracture surface. Red solid arrows indicate peeling of graphitic layers from the AG tetrapod.

However, pull-out of the arms is not the only phenomenon that was observed on the fracture surfaces. Figs. 7a and b reveals a closer view on one the pulled out arms of the Aerographite. It can be seen that there are ripples on the outer sheet like layer, which surrounds the epoxy matrix (indicated by red solid arrow) and this very similar to the telescopic pull-out/sword-in-sheath mechanism observed for CNT/epoxy composites. However, as stated above, such a mechanism for CNTs could occur in case of a strong interface and in contrast, AG/epoxy exhibits pull-out as a result of a weak interface and these ripples on the AG are in fact graphitic layers that start to tear due to the shear in between the graphitic layers. It must be noted that the AG arm do not comprise of monolayer graphene but a stack of graphene layers. The ripples observed in the arms tear as concentric rings, which is due to the formation/growth process of AG from ZnO templates

in the CVD reactor. The bottom right corner of Fig. 7a (indicated by solid red arrow) confirms that the epoxy matrix is engulfed by the graphitic layers of AG. Nevertheless, it is still unclear from the pull-out of the arms, whether all the graphitic layers are completely de-bonded from the matrix.

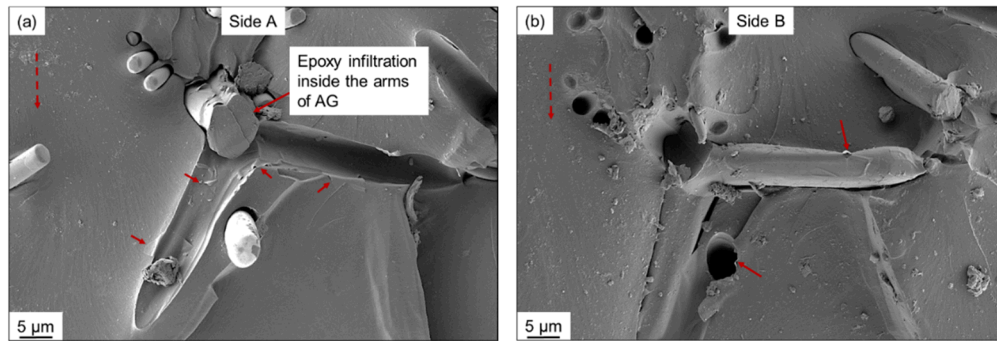


Figure 8: Scanning electron micrograph of a single AG tetrapod fractured at the base (a) epoxy infiltrating inside the AG tetrapod and red arrows indicate the peeled graphene layers on the impression of the pulled out AG tetrapod and (b) outer graphitic layers still remain intact in the epoxy matrix on the de-bonded site.

The above scanning electron micrograph is just one example, which clearly reveals that the AG arms that are hollow in nature are infiltrated by epoxy as indicated in Fig. 8a. The fracture surface of epoxy can be easily distinguished from that of graphene layers. The fracture at the base of AG tetrapod, contains the fractured epoxy and shows the flow patterns that are distinct features of brittle epoxies. This shows that the slow vacuum assisted infiltration process in the preparation of AG/epoxy composite is successful. A closer observation on the de-bonded area of the arms of AG, the small red arrows in Fig. 8a and b point out that the outer graphitic layers are still bonded with the matrix, and the rest of the layers can be found on the de-bonded arm. This peeling of graphitic layers is because of the shearing in between the layers due to the weak van der Waals forces. The observed separation in-between the graphitic layers of AG tetrapod is typical for layered nano-fillers and Similar mechanism has been reported for nano-clay/epoxy

and graphene/epoxy composites [30–32]. The observed ripples on the arms of AG are found to be graphitic in nature; confirmed through Raman Spectroscopy.

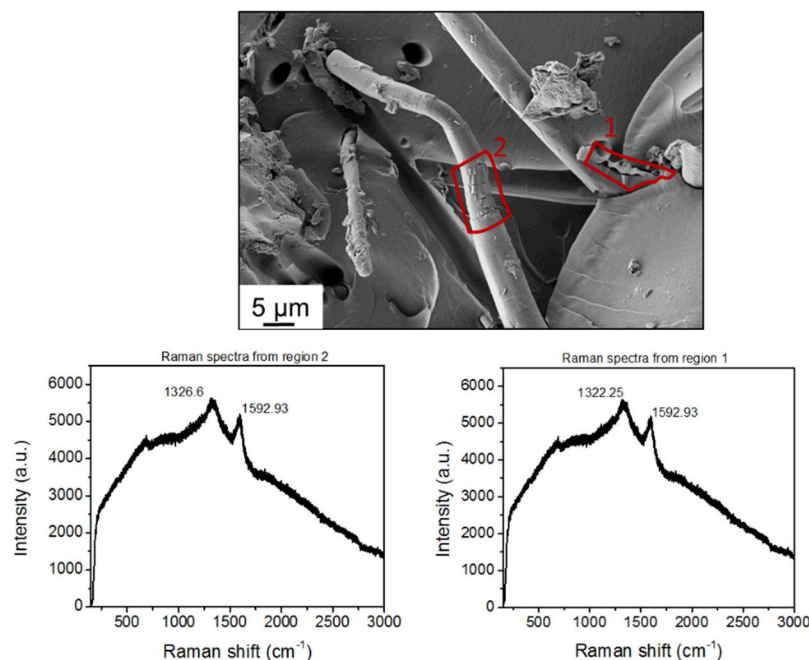


Figure 9: Raman spectra of the ripples observed on AG tetrapod in the fracture surface of AG/epoxy composite at two different regions along with the scanning electron micrograph.

For better understanding, the regions on which the Raman spectra was recorded is marked with an outline. The Raman spectra shown in Fig. 9 are not corrected for background subtraction and the large scattering from background comes from epoxy (matrix). On close observation, two distinct peaks at 1326/1322 cm^{-1} and 1592/1592 cm^{-1} are observed from both the regions of interest. The two peaks correspond to the D and G band associated with graphitic layers. For reference similar Raman spectra were taken on the arms of as-prepared AG (prior infiltration) and their D and G band values correspond to 1322 and 1586 cm^{-1} respectively (see supplementary info Fig. S3). This assures that the ripples or peeled layers from the AG tetrapod are graphitic. Nevertheless, from the observed Raman data, it is very difficult to estimate the number of layers that were separated upon shearing. The red arrow in Fig. 8b points to the

impression of a pull-out where a graphitic layer is sticking out; this adds to the evidence that a complete de-bonding of the arms does not occur; whereas, graphitic layers are separated during failure and a few of the layers remain on the de-bonded site. This kind of failure was also observed in other type of graphene foams [23]. It is now ascertained from fractographic analysis through SEM, that there is separation in between the graphitic layers and in the AG tetrapod and pull-out of the arms is the two main dominant failure mechanisms that contribute to fracture.

4.1.2 Photoelasticity on AG/epoxy model composite

In-situ tensile tests under polarised light microscope on the model composite AG/epoxy thin film tensile test coupon containing a crack gave further insight on the interaction of the crack front with an AG agglomerate when subjected to tensile forces. From Fig. 10, the process zone at the tip of the crack and scattered agglomerates of AG tetrapod are clearly visible. Owing to the limitations of height adjustment in the in-situ fixture, obtaining higher magnified optical micrographs was not possible. The sample with initial crack is given at the top left corner while the Figs. 10a-i shows the magnified image near the crack tip for better viewing.

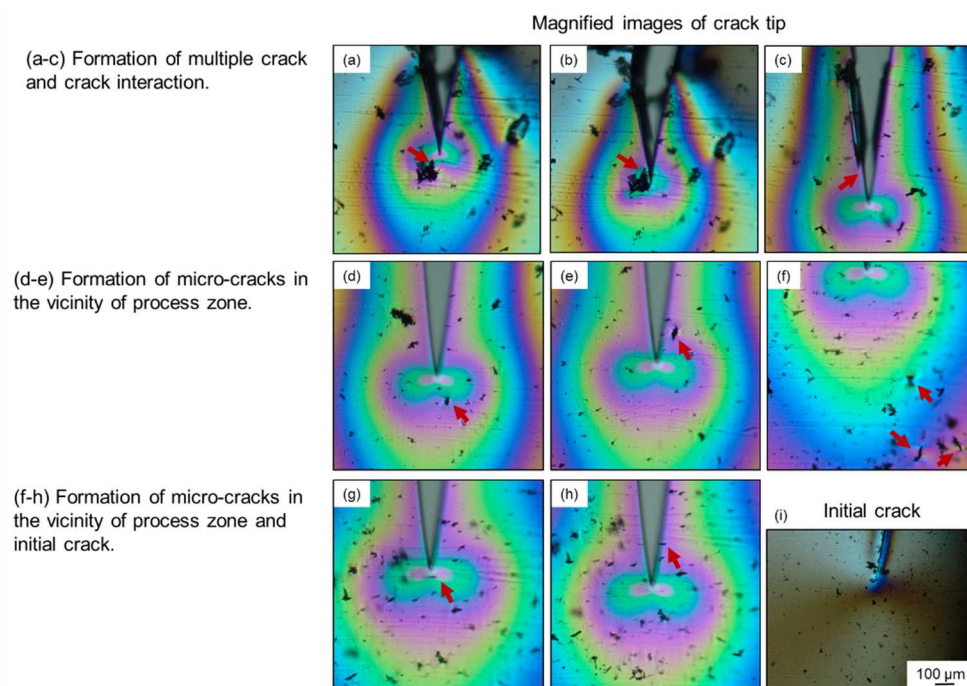


Figure 10: Isochromatic fringe pattern (white light) of AG/epoxy thin film model composite showing multiple cracks, micro-cracks ahead of the main crack in the process zone and pull-out of a single AG tetrapod.

Fig. 10 contains magnified images of the crack tip with initial crack inserted in the sample (Fig. 10i) and its propagation through the model composite when subjected to tensile load. Upon loading, a micro-crack is developed near the process zone near the AG agglomerate as in Fig. 10a. As the crack starts to propagate, the developed micro-crack, runs backward to join the main crack (Fig. 10b) and this is defined by the term “crack interaction” and then later continues to propagate along with the main crack with a delayed crack propagation (Fig. 10c). When the same test was performed on another sample with a larger agglomerate of AG interacting with the crack tip, multiple cracks were observed after passing through the agglomerate (see supplementary info, Fig. S5). Further, in Fig. 10d and 10e, one could see the influence of the process zone on an AG agglomerate ahead of the main crack tip, which upon loading and crack propagation causes micro-crack. The geometry of the generated micro-crack points again to crack-interaction and this feature was also observed in graphene/epoxy composite. This ascertains our observed feature of inter-graphitic layer separation in the fracture surface of AG/epoxy. The formation of the micro-crack is observed at several places in the sample and this is the result of the influence of the process zone on the neighbouring particles causing inter-graphitic layer separation (Fig.10f). This shows a larger dissipation of energy because of the 3D interconnected morphology of AG. However, this was not visible as a greater increment in fracture toughness, the experimental observations from the model composite shows the potential of using AG as a reinforcement in polymeric matrix. Another feature of pull-out of AG tetrapod that was seen in the fracture surface was also observed in the in-situ tensile test on model composite. In Fig. 10g, the red

arrow points to a single AG arm oriented perpendicular to the main crack and the arm is pulled out from the matrix as the crack passes through it (Fig. 10h).

5 Conclusion

The present work shows that Aerographite, which is a lightweight variant within the 3D network structures, can be infiltrated with epoxy to obtain a nano-composite without damaging the 3D interconnected structure of AG. Preliminary tests on these composites showed their ability to improve the mechanical properties of epoxy matrix at very low filler content. A detailed fractographic analysis on these composites show pull out of the arms due to interface failure and inter-graphitic failure through shear in between the graphitic layers as major failure mechanisms.

Although, an enhancement of 19 % in fracture toughness was observed in these composites, they exhibited an increase in energy absorption under uni-axial compression. The observed mechanical properties can be optimised by tuning the presence of remnant ZnO impurities in AG, number of graphitic layers (wall thickness) of AG.

The work also uses photoelasticity observations on AG/epoxy model composite to understand better the interaction of a crack and its process zone on the neighbouring AG particles. Formation of micro-cracks in a dense AG agglomerate ahead of the main crack and its interaction with main crack result in formation of multiple cracks. Thereby concluding that the 3D interconnected structure of AG also enhances the mechanical properties apart from increased electrical conductivity exhibited by these composites. Further work will focus on tuning the quality and morphology of as-prepared AG for a systematic study on the effect of morphology on the mechanical and electrical properties of AG/epoxy composites.

6 Acknowledgement

The authors would like to acknowledge Ms. Svenja Garlof for her help in the synthesis of Aerographite, Mr. Daniel Fritsch, Mr. Karthik Nageshwara Rao (student assistant) for their support in composite preparation and Ms. Evie Chalmers (summer intern student) for compression testing. We would also like to acknowledge European Union Seventh Framework Programme under grant agreement n°604391 Graphene Flagship for the financial support. The co-author Mr. Matthias Mecklenburg would like to acknowledge German Research Foundation (DFG) via SFB 986 M³, project B1 for funding his work at TUHH.

Prepared by LLNL under Contract DE-AC52-07NA27344

References

- [1] Mecklenburg M, Schuchardt A, Mishra YK, Kaps S, Adelung R, Lotnyk A et al. Aerographite: Ultra lightweight, flexible nanowall, carbon microtube material with outstanding mechanical performance. *Advanced Materials* 2012;24(26):3486–90.
- [2] Novoselov KS, Fal'ko VI, Colombo L, Gellert PR, Schwab MG, Kim K. A roadmap for graphene. *Nature* 2012;490(7419):192–200.
- [3] Chatterjee S, Nafezarefi F, Tai NH, Schlagenhaut L, Nüesch FA, Chu B. Size and synergy effects of nanofiller hybrids including graphene nanoplatelets and carbon nanotubes in mechanical properties of epoxy composites. *Carbon* 2012;50(15):5380–6.
- [4] Galindo B, Alcolea SG, Gómez J, Navas A, Murguialday AO, Fernandez MP et al. Effect of the number of layers of graphene on the electrical properties of TPU polymers. *IOP Conference Series: Materials Science and Engineering* 2014;64:12008.
- [5] Potts JR, Dreyer DR, Bielawski CW, Ruoff RS. Graphene-based polymer nanocomposites. *Polymer* 2011;52(1):5–25.
- [6] Kim H, Abdala AA, Macosko CW. Graphene/Polymer Nanocomposites. *Macromolecules* 2010;43(16):6515–30.
- [7] Young RJ, Kinloch IA, Gong L, Novoselov KS. The mechanics of graphene nanocomposites: A review. *Composites Science and Technology* 2012;72(12):1459–76.
- [8] Chabot V, Higgins D, Yu A, Xiao X, Chen Z, Zhang J. A review of graphene and graphene oxide sponge: material synthesis and applications to energy and the environment. *Energy and Environmental Science* 2014;7(5):1564.
- [9] Xia X, Chao D, Fan Z, Guan C, Cao X, Zhang H et al. A new type of porous graphite foams and their integrated composites with oxide/polymer core/shell nanowires for supercapacitors: Structural design, fabrication, and full supercapacitor demonstrations. *Nano Letters* 2014;14(3):1651–8.

- [10] Zhao J, Ren W, Cheng H. Graphene sponge for efficient and repeatable adsorption and desorption of water contaminations. *Journal of Materials Chemistry* 2012;22(38):20197.
- [11] Hong J, Bak BM, Wie JJ, Kong J, Park HS. Reversibly Compressible, Highly Elastic, and Durable Graphene Aerogels for Energy Storage Devices under Limiting Conditions. *Advanced Functional Materials* 2015;25(7):1053–62.
- [12] Dong X, Wang X, Wang L, Song H, Zhang H, Huang W et al. 3D graphene foam as a monolithic and macroporous carbon electrode for electrochemical sensing. *ACS Applied Materials & Interfaces* 2012;4(6):3129–33.
- [13] Ye S, Feng J, Wu P. Deposition of three-dimensional graphene aerogel on nickel foam as a binder-free supercapacitor electrode. *ACS Applied Materials & Interfaces* 2013;5(15):7122–9.
- [14] Jia J, Sun X, Lin X, Shen X, Mai Y, Kim J. Exceptional Electrical Conductivity and Fracture Resistance of 3D Interconnected Graphene Foam/Epoxy Composites. *ACS Nano* 2014;8(6):5774–83.
- [15] Chen Z, Xu C, Ma C, Ren W, Cheng H. Lightweight and Flexible Graphene Foam Composites for High-Performance Electromagnetic Interference Shielding. *Advanced Materials* 2013;25(9):1296–300.
- [16] Chen G, Liu Y, Liu F, Zhang X. Fabrication of three-dimensional graphene foam with high electrical conductivity and large adsorption capability. *Applied Surface Science* 2014;311:808–15.
- [17] Li Y, Samad YA, Polychronopoulou K, Alhassan SM, Liao K. Highly Electrically Conductive Nanocomposites Based on Polymer Infused Graphene Sponges. *Scientific Reports* 2014;4.
- [18] Chen G, Liu Y, Liu F, Zhang X. Fabrication of three-dimensional graphene foam with high electrical conductivity and large adsorption capability. *Applied Surface Science* 2014;311:808–15.
- [19] Reddy SK, Ferry DB, Misra A. Highly compressible behavior of polymer mediated three-dimensional network of graphene foam. *RSC Advances* 2014;4(91):50074–80.
- [20] Wu C, Huang X, Wu X, Qian R, Jiang P. Mechanically flexible and multifunctional polymer-based graphene foams for elastic conductors and oil-water separators. *Advanced Materials* 2013;25(39):5658–62.
- [21] Zhao Y, Liu J, Hu Y, Cheng H, Hu C, Jiang C et al. Highly compression-tolerant supercapacitor based on polypyrrole-mediated graphene foam electrodes. *Advanced Materials* 2013;25(4):591–5.
- [22] Samad YA, Li Y, Schiffer A, Alhassan SM, Liao K. Graphene foam developed with a novel two-Step technique for low and high strains and pressure-sensing applications. *Small* 2015:1–6.
- [23] Wang Z, Shen X, Akbari Garakani M, Lin X, Wu Y, Liu X et al. Graphene aerogel/epoxy composites with exceptional anisotropic structure and properties. *ACS Applied Materials & Interfaces* 2015:150227143151006.

- [24] Peng Q, Li Y, He X, Gui X, Shang Y, Wang C et al. Graphene nanoribbon aerogels unzipped from carbon nanotube sponges. *Advanced Materials* 2014;26(20):3241–7.
- [25] Hu H, Zhao Z, Zhang R, Bin Y, Qiu J. Polymer casting of ultralight graphene aerogels for the production of conductive nanocomposites with low filling content. *Journal of Materials Chemistry A* 2014;2(11):3756.
- [26] E A Patterson and Z F Wang. Towards full field automated photoelastic analysis of complex components. *Strain* 1991;27(2):49–53.
- [27] Fiedler B, Hojo M, Ochiai S, Schulte K, Ando M. Failure behavior of an epoxy matrix under different kinds of static loading. *Composites Science and Technology* 2001;61(11):1615–24.
- [28] Ashby M. The properties of foams and lattices. *Philosophical Transactions of the Royal Society A: Mathematical, Physical and Engineering Sciences* 2006;364(1838):15–30.
- [29] Florian H. Gojny Malte H.G. Wichmann, Bodo Fiedler, Karl Schulte. Influence of different carbon nanotubes on the mechanical properties of epoxy matrix composites – A comparative study. *Composites Science and Technology* 2005;65:2300–13.
- [30] Chandrasekaran S, Sato N, Tölle F, Mülhaupt R, Fiedler B, Schulte K. Fracture toughness and failure mechanism of graphene based epoxy composites. *Composites Science and Technology* 2014;97:90–9.
- [31] Wang K, Chen L, Wu J, Toh ML, He C, Yee AF. Epoxy nanocomposites with highly exfoliated clay: Mechanical properties and fracture mechanisms. *Macromolecules* 2005;38(3):788–800.
- [32] Zaman I, Phan TT, Kuan H, Meng Q, Bao La, Ly Truc, Luong L et al. Epoxy/graphene platelets nanocomposites with two levels of interface strength. *Polymer* 2011;52(7):1603–11.